The promotion effect of aluminium ion on hydrogen entry into steel during atmospheric corrosion

Xiaole Han [a,*] and Masatoshi Sakairi [b]

[a] Graduate School of Engineering, Hokkaido University, Kita-13, Nishi-8, Kita-ku, Sapporo 060-8628, Japan. E-mail address: hansyole@eis.hokudai.ac.jp

[b] Faculty of Engineering, Hokkaido University, Kita-13, Nishi-8, Kita-ku, Sapporo 060-8628, Japan. E-mail address: msakairi@eng.hokudai.ac.jp

[*] Corresponding author.

E-mail address: hansyole@eis.hokudai.ac.jp

Postal address: MC810, Graduate School of Engineering, Hokkaido University, Kita-13, Nishi-8, Kita-ku, Sapporo 060-8628, Japan

Abstract

The effect of Al^{3+} on the hydrogen permeation behaviour of steel during cyclic corrosion was investigated under $AlCl_3$ droplets with varying Al^{3+} concentrations. The permeated hydrogen during the corrosion process was measured by electrochemical techniques. The observation of corrosion morphology and analysis of corrosion products were performed in the corrosion tests. It was found that Al^{3+} presented a significant effect on corrosion morphology and hydrogen entry into steel. The amount of permeated hydrogen through steel increased with increasing Al^{3+} concentrations. The precipitation of Al species under salt droplets, the localized acidification under rust layers, and the hygroscopic property of $AlCl_3$ were considered contributing factors enhancing the hydrogen evolution and absorption into steel during wet-dry cyclic corrosion.

Keywords

High strength steel

Aluminum chloride

Atmospheric corrosion

Hydrogen absorption

Hydrogen permeation

1. Introduction

Steel products used in atmospheric environments are susceptible to corrosion damage as aqueous aerosols bring moisture into contact with the steel surface [1]. When aluminium (Al) containing coatings are employed to protect steel against corrosion attack, the dissolved Al^{3+} from the coatings participates in the corrosion process, introducing hygroscopic species such as $AlCl_3$ in atmospheric corrosion [2-4]. The deposited $AlCl_3$ absorbs moisture and provides a conductive electrolyte layer on the steel surface, where atmospheric corrosion occurs as an electrochemical process. Hydrogen evolution is a prominent reaction during the corrosion process and produces a considerable amount of atomic hydrogen [5-9]. Subsequently, a portion of the produced hydrogen enters the steel, presenting a cracking risk to the steel components [10]. Thus, the participation of Al^{3+} is a significant consideration for investigating hydrogen entry into steel during atmospheric corrosion.

Atmospheric corrosion is generally regarded as a cyclic wet-dry process attributed to the varying relative humidity (RH) and temperature [11,12]. Once the surrounding RH rises above the deliquescence RH (DRH) of the deposited salts, the electrolyte layers are available on the steel surface [13]. Schindelholz et al. [14,15] investigated the relationship between RH and the corrosion response of mild steel contaminated with NaCl (DRH: 76%) and $MgCl_2$ (DRH: 33%) particles and reported that $MgCl_2$ achieved sustained corrosion under a lower RH than NaCl. Based on this finding, Schimo-Aichhorn et al. [16] reported that $MgCl_2$ deposits prolonged the hydrogen insertion into steel more than NaCl during atmospheric corrosion. These results suggest a hypothesis that hygroscopic salts with low DRH provide a prolonged duration for corrosion and hydrogen entry into steel. As $AlCl_3$ is highly

hygroscopic with a DRH of 30% [17,18], it is necessary to determine whether this hypothesis applies to $AlCl_3$.

In addition to the deliquescence property of the hygroscopic salts, the dissolved metal cations participate in the corrosion process and significantly influence the corrosion kinetics. Regarding the corrosion process of steel under salt deposits, the anodic iron dissolution and cathodic oxygen reduction reaction (ORR) are expected to produce a pH gradient in the electrolyte film [19]. The higher concentration of OH^- in the cathodic area is favourable for the migration of dissolved metal cations, resulting in the formation of precipitates that block the cathodic sites [20-23]. Moreover, the dissolved metal cations have been shown to incorporate into the oxide films and exhibit different abilities to protect the metal from corrosion [24-28]. Although the retardation of the corrosion process by the dissolved metal cations is expected to hinder the hydrogen uptake of steel, various cations have been reported to enhance the hydrogen evolution reaction (HER) on the cathode surface [29-31]. Liu et al. [29] reported that Al^{3+} had an acceleration effect on HER by facilitating the transport of the proton through the Al oxide/hydroxide film precipitated on the substrate surface. These results imply the significant role of Al^{3+} in hydrogen evolution during the corrosion process.

The purpose of this study is to explore the influence of Al^{3+} on the hydrogen uptake of steel during atmospheric corrosion. The hydrogen permeation behaviour of steel under salt droplets with varying Al^{3+} concentrations was investigated to assess the importance of the hygroscopic property of $AlCl_3$ and the role of Al^{3+} in hydrogen absorption during cyclic wet-dry corrosion.

2. Experimental

2.1 Sample preparation

The samples with dimensions of 20 mm × 15 mm × 1 mm were cut from a Cr-Mo steel bar (C: 0.35, Si: 0.18, Mn: 0.74, P: 0.0011, S: 0.0017, Cr: 1.15, Mo: 0.15, Fe: balance, all in mass%), as illustrated in Fig. 1. The surfaces of the steel samples were mechanically ground up to 2400 grit using silicon carbide papers. The polished samples were cleaned ultrasonically with ethanol and ultrapure water for 300 s, respectively, and then dried with flowing air before the tests.

2.2 Hydrogen permeation and cyclic corrosion tests

An electrochemical setup consisting of an upper exposed area for corrosion occurrence and a lower electrochemical cell for hydrogen detection was employed to detect the atomic hydrogen that diffused through the samples during cyclic corrosion. One side of the sample was electroplated with about 1 μm thick Ni in a 0.312 M $NiSO_4$/0.781 M H_3BO_3 solution at 4 mA cm^{-2} for 720 s. The Ni-plated side was attached to the hydrogen detection cell, acting as the working electrode (WE). The counter and reference electrodes (CE and RE) were made of Pt wires (diameter: 0.5 mm), and the electrolyte was 1 M NaOH solution. The sample was polarized at a constant anodic potential of -30 mV vs. Pt using a potentiostat (HECS 318C, Fuso, Kawasaki, Japan). This potential was sufficient to ensure rapid ionization of the atomic hydrogen that diffused through the sample. The changes in the anodic current of the detection cell were recorded during the cyclic corrosion test. In addition, the background current was recorded without performing corrosion upon the sample and subtracted from the detected

hydrogen permeation currents to eliminate the interference of temperature on the anodic current fluctuation.

The other side of the sample was performed as the corrosion side and exposed to the external environment. A droplet of 10 μL salt solution was placed on the sample surface to initiate corrosion. The salt solutions used in the tests are listed in Table 1, which were prepared using analytic grade reagents (Kanto Chemical Co., Inc., Japan) and ultrapure water at room temperature. The concentration of Cl^- was 10 mM in each solution. After the placement of the aqueous salt solutions, the changes in temperature and humidity surrounding the samples were controlled using a chamber (IW243, Yamato Scientific Co., Ltd., Japan) according to a procedure of wet (1 h), drying (1 h), dry (3 h), and wetting (1 h) in one cycle (6 h). Each corrosion test was conducted for 12 consecutive cycles (72 h).

2.3 Potentiodynamic polarization test

The potentiodynamic polarization data of the samples at various stages of a wet-dry corrosion cycle were of interest in the present work, including the as-polished sample, and the corroded samples after the wet (1 h) and drying (1 h) stages under aqueous salt droplets (10 mM NaCl and 3.33 mM $AlCl_3$), respectively. The samples were mounted in resin with an exposure area of 28.27 mm^2 for droplet deposition. After the corrosion tests under corresponding conditions, the polarization curves of the samples were measured in a three-electrode electrochemical cell with the samples as WE, a platinum plate (2cm × 2cm) as CE, and an Ag/AgCl electrode (SSE) immersed in a saturated KCl solution as RE. Note that the corroded surfaces were cleaned using ultrapure water to remove the residual droplets before

the electrochemical measurements. The measurements were carried out in 10 mM NaCl solution and performed using a potentiostat (PocketSTAT, Ivium Technologies, Netherlands). After the measurement of open-circuit potential for 1 h at room temperature, the potential scan was performed at a rate of 1 mV/s in the cathodic and anodic directions to obtain individual polarization curves.

2.4 Surface characterisation and analysis

The changes in the surface morphology of the samples during the cyclic corrosion process were recorded using a USB camera connected to a personal computer. An optical microscope (OM, MV-550, WRAYMER Inc., Japan) was used to observe the micrographs of the corroded surfaces. The corrosion products were characterized using a scanning electron microscope (SEM, JSM-6510-LA, JEOL Ltd., Japan) and analysed using an energy-dispersive X-ray spectrometer (EDS) with accelerating voltages of 10 kV and 20 kV, respectively. The cross-sectional samples were prepared using a cross-section polisher (IB-19520CCP, JEOL Ltd., Japan) and characterized using SEM. An auger electron spectrometer (AES, JAMP-9500F, JEOL Ltd., Japan) was used to analyse the corrosion product layer with an accelerating voltage of 10 kV, a spatial surface resolution of about 6 nm, and a probe diameter of about 10 nm. Note that the samples were cut into smaller sizes using a cutting machine and cleaned with ultrapure water prior to the AES analysis.

3. Results and discussion

3.1 Hydrogen entry into steel under $AlCl_3$ droplet during cyclic corrosion

The atmospheric corrosion process of steel induced by salt deposits can be divided into two stages: the corrosion under the initial salt droplets and the corrosion under the rust layers after the water evaporates. Therefore, the present study investigated the hydrogen permeation behaviour of steel during the above two stages of cyclic corrosion.

Fig. 2 shows a typical record of the hydrogen permeation current density of the sample exposed to 3.33 mM $AlCl_3$ droplet during 12 consecutive cycles (72 h). In the first cycle (Fig. 2(a)), the current increases gradually during the initial wet period, implying the occurrence of hydrogen absorption into the sample. In the subsequent drying period, the current increases prominently as RH decreases and temperature increases, which indicates that the drying condition accelerates the hydrogen evolution and entry into steel during the corrosion process. When the environment is constant at a high temperature and a low RH, the current reaches a maximum value and then decreases at a rapid rate in the dry period. This phenomenon suggests the retardation of hydrogen absorption into the sample. In the final wetting period, the current declines initially due to the decrease in temperature, and then exhibits a hump-shaped change, indicating that the increase in RH facilitates the hydrogen entry process.

In the subsequent cycles (Fig. 2(b)), the current curves exhibit a similar variation during the wet-dry cycles. The currents begin to increase significantly in the drying period and then decrease after the steel surfaces become dry. The variations in the curves indicate that no appreciable amount of permeated hydrogen exists during the wet period, and the hydrogen entry process mainly happens in the drying period of cyclic corrosion. The increasing temperature and decreasing RH are contributing factors for hydrogen evolution and absorption reactions. As the wet-dry cycle increases, the maximum current values represent a

monotonic decrease, and the currents tend to be identical after 11 cycles regardless of the changes in RH and temperature. These phenomena suggest that the hydrogen absorption processes gradually stagnate with the increase of cycle number.

3.2 Comparison of hydrogen entry into steel under salt droplets with varying Al^{3+} concentrations

In an attempt to investigate the role of Al^{3+} in hydrogen entry into steel during cyclic corrosion, the present study examined the hydrogen permeation behaviour of the samples exposed to four kinds of salt droplets with varying Al^{3+} concentrations. As shown in Fig. 3, the amount of permeated hydrogen is obtained by integrating the permeation current density with respect to the durations of wet-dry cycles. The twelve consecutive cycles are rearranged into an individual first cycle and a sum of the subsequent cycles in consideration of the mentioned two stages of atmospheric corrosion.

In the first cycle, the corrosion processes start and proceed under the initial salt droplets, accompanied by hydrogen absorption into the samples. The amount of permeated hydrogen through the samples increases with increasing concentrations of Al^{3+} (Fig. 3(a)). The results suggest that the presence of Al^{3+} plays an important role in the hydrogen absorption process during the corrosion under the initial droplet. The higher the concentration of Al^{3+} in the droplet, the higher the activity of hydrogen absorption into steel. After eleven wet-dry cycles (Fig. 3(b)), the amount of permeated hydrogen through the samples as a function of the concentration of Al^{3+} presents a similar characteristic compared to the first cycle. A particular difference is that the amount of permeated hydrogen at high Al^{3+} concentrations is

significantly greater than that at low Al^{3+} concentrations. These results indicate that Al^{3+} still exhibit an acceleration effect on hydrogen entry into steel during the corrosion process under the rust layers. However, it is noticeable that the amount of permeated hydrogen in the subsequent eleven cycles is slightly larger than in the first cycle. This finding suggests that the hydrogen entry mainly occurs in the initial wet-dry cycle under salt droplets.

3.3 Corrosion morphology of steel during cyclic corrosion

To investigate the relationship between the corrosion morphology and hydrogen entry into steel, this study observed the surface changes of the samples during the cyclic corrosion tests. After the deposition of salt droplets, two typical changes in the corrosion morphology of samples are displayed in Fig. 4, selected for exposure to (a) a mixed salt solution (1 mM $AlCl_3$ + 7 mM NaCl) and (b) 3.33 mM $AlCl_3$.

3.3.1 Corrosion morphology under the initial droplets

The deposited salt solutions have apparent droplet shapes at the beginning of the corrosion test. Within half an hour after the initiation of the wet-dry process, no perceptible corrosion products appear on the sample surfaces, and the droplets tend to spread outward and cover the exposed surfaces. At the end of the wet period (1 h), considerable amounts of yellow corrosion products develop and accumulate along the peripheral region of the NaCl-containing droplet, forming a ring-shaped rust layer (Fig. 4(a), white arrow). This typical phenomenon has been observed in abundant literature [32-35], attributed to the different oxygen concentrations between the central and peripheral regions under the droplet. The

central region, where the oxygen concentration is low, is supposed to act as an anodic site for iron dissolution. Ferrous ions released from the anodic sites migrate to the peripheral region, where ORR takes place, and encounter hydroxide ions to form corrosion products.

On the other hand, the corrosion morphology under the droplet containing 3.33 mM $AlCl_3$ exhibits a distinct difference from the droplet containing NaCl. An appreciable black spot (Fig. 4(b), white arrow) exists in the central area in preference to the formation of an apparent rust ring in the peripheral area of the droplet. Considering the oxygen concentration difference in the droplet, the central spot is supposed to be the anodic region. Al^{3+} is expected to migrate to the peripheral cathodic region and precipitate within an appropriate pH range, forming a slight white layer on the sample surface (Fig. 4(b), red arrow) instead of abundant yellow corrosion products observed under the NaCl-containing droplet. This precipitated white layer has been shown to accelerate HER in the cathodic region [29], which facilitates hydrogen entry into steel when the corrosion proceeds under the $AlCl_3$ droplet.

In the subsequent drying period, the amounts of corrosion products under the NaCl-containing droplet increase as water evaporates. However, the changes in surface morphology under the $AlCl_3$ droplet are apparently different from the NaCl-containing droplet, manifested by no appreciable change in the amounts and colour of the corrosion products. The increase in the concentration of Al^{3+} retards the formation of corrosion products under the droplet. Combining the results of the hydrogen permeation tests, the increase in the concentration of Al^{3+} accelerates hydrogen entry regardless of the amounts of corrosion products during the corrosion processes. These findings suggest that the hydrogen absorption reaction becomes active after the formation of Al-containing precipitated films rather than the common yellow

corrosion products. When corrosion occurs under $AlCl_3$ droplets, the HER is supposed to become active in the cathodic region, resulting in an increase in the number of absorbed hydrogen atoms.

3.3.2 Corrosion morphology after the evaporation of droplets

After the droplets evaporate, the sample surfaces become visibly dry, and the corrosion processes are supposed to be hindered by the absence of electrolyte layers. However, new corrosion products can be found along the peripheral regions of the exposed surface (Fig. 4(b), yellow arrows). Although 20% RH is much lower than the DRH of $AlCl_3$ particles and no electrolyte is expected, corrosion can still proceed under the rust layers. As the RH increases and temperature decreases to the wet conditions, noticeable new corrosion products can be found on the sample under the $AlCl_3$ droplet. Combining the hydrogen permeation results, the mentioned hump-shaped change in the current curve during the first wetting period (Fig. 2(a)) can be attributed to an initial increase in the amount of electrolyte, which accelerates corrosion and hydrogen absorption, and a subsequent decrease in the concentration of corrosive ions, which retards corrosion and hydrogen entry into steel.

In the subsequent second and third cycles, there is a perceptible increase in the amounts of brown corrosion products on the sample surfaces. Since no extra water was supplied to the exposed surfaces during the cyclic corrosion tests, the deposited salt particles in the rust layers are supposed to absorb moisture and facilitate corrosion and hydrogen entry into samples. As the number of corrosion cycles increases, the increased thickness of the rust layers makes it difficult for the electrolytes produced from the salts to reach the steel surface

through the thick rust layers. The decrease in the thickness of electrolytes on the steel inhibits the corrosion processes, resulting in a decrease in the amount of permeated hydrogen (Fig. 2(b)). In addition to the rust layers, the deliquescent ability of the deposited salts is also responsible for the thickness of the electrolyte layer. As $AlCl_3$ can absorb water and deliquesce more easily than NaCl, the increase in the amount of permeated hydrogen with increasing concentration of Al^{3+} (Fig. 3(b)) is attributed to the increase in the amount of the deposited $AlCl_3$, which increases the volume of the electrolytes and provides an extended duration for corrosion and hydrogen entry into steel.

Together, the changes in the amount of permeated hydrogen and surface morphology suggest that the increase in the amount of permeated hydrogen through steel under $AlCl_3$ droplets is related to the acceleration of HER by the precipitation of Al compounds in the cathodic region. After the droplets evaporate, the high ability of the deposited $AlCl_3$ to absorb moisture contributes to the formation of electrolytes for corrosion and hydrogen absorption activities.

3.4 Electrochemical kinetics of steel in different stages of corrosion

As the samples under droplets with varying Al^{3+} concentrations exhibited considerable discrepancy in the corrosion morphology and hydrogen permeation behaviour, this study measured the electrochemical kinetics of the samples at various stages of the first corrosion cycle, including the corroded samples after the drying stage (2 h) under (a) 3.33 mM $AlCl_3$ and (b) 10 mM NaCl, the corroded samples after the wet stage (1 h) under (c) 3.33 mM $AlCl_3$ and (d) 10 mM NaCl, and (e) the as-polished samples.

Fig. 5 shows the polarization curves of the samples that were corroded under salt droplets after different stages of a wet-dry cycle. Prior to the electrochemical measurements, the corroded samples were cleaned with ultrapure water to remove the residual droplets and unconsolidated corrosion products. The cathodic kinetics of the samples at different stages display distinct differences in the diffusion-limited current densities (DLCD). DLCD for the samples corroded under 10 mM NaCl droplets is smaller than that under 3.33 mM $AlCl_3$ droplets after the same corrosion durations. Apart from the reduction reaction of dissolved oxygen in the electrolyte, the increase in the cathodic current density is suggested to be attributed to the reduction reactions of iron rust on the corroded surfaces, involving the conversion of FeOOH to Fe_3O_4 [8,36,37]:

$$3FeOOH + e^- \rightarrow Fe_3O_4 + H_2O + OH^- \quad (1)$$

Therefore, the larger amount of adherent iron rust on the sample surfaces might be responsible for the stronger cathodic kinetics of the samples in the polarization tests.

Although the amounts of corrosion products under NaCl-containing droplets are greater than that under $AlCl_3$ droplets (Fig. 4), it should be noted that the corroded samples were cleaned with ultrapure water prior to the measurements. The corrosion products under NaCl droplets were unconsolidated on the sample surfaces and easily removed by ultrapure water. In contrast, the generated corrosion products under $AlCl_3$ droplets adhered tightly to the sample surfaces, contributing to the cathodic kinetics of the corroded samples in the polarization tests. These results demonstrate the positive role of Al^{3+} in the formation of adherent rust layers on steel during corrosion under salt droplets. Furthermore, DLCD for the samples corroded under salt droplets after the drying stage (2 h) is greater than that after the

wet stage (1 h). The increase in the amounts of corrosion products after the drying stage is considered to be responsible for the increasing DLCD.

Another characteristic of the polarization curves is the difference in the corrosion potentials of the samples. The corrosion potential of the sample under (a) $AlCl_3$ after the drying stage is nobler than that under (b) NaCl, attributed to the suppression of anodic dissolution after the formation of precipitates on the sample under $AlCl_3$ droplets. This is consistent with the observation results that no prominent increase in the amounts of corrosion products appears on the sample surfaces (Fig. 4(b)).

In summary, the polarization data demonstrate that the amount of adherent corrosion products under $AlCl_3$ is larger than that under NaCl, attributing to the precipitation of Al compounds. In addition, the Al-containing precipitated films are suggested to retard the initial dissolution of iron under $AlCl_3$ droplets. These results corroborate the findings that Al^{3+} can introduce a precipitated layer on the steel, suppressing iron dissolution while accelerating hydrogen absorption during the corrosion of steel under $AlCl_3$ droplets.

3.5 Sectional analysis of corroded surfaces after cyclic corrosion

In addition to the corrosion process and hydrogen absorption under the initial salt droplets, hydrogen entry that occurs after the droplets evaporate and the rust layers cover the steel surfaces is also noticeable in cyclic corrosion. To determine the influence of Al^{3+} on the corrosion activity under the rust layers, the corrosion products were carefully removed from the samples that were corroded for 12 cycles. Fig. 6 shows the optical images of the corroded samples and the images after removing the corrosion products. The corrosion products of the

samples under different deposited salts present different characteristics. In the case of the sample corroded under a mixed salt solution with a high Na^+ concentration, a large proportion of corrosion products are yellow and relatively flat, and the raised brown ones prefer to form towards one side of the exposed surface, attributed to the airflow inside the chamber. Regarding the sample corroded under the $AlCl_3$ droplet, the exposed surface shows a distinctive rust spot near the central region (Fig. 6(b), white arrow) and a ring-shaped rust layer along the peripheral region (Fig. 6(b), yellow arrow). The brown corrosion products in hump shapes occupy a greater portion of the exposed surface.

After removing the rust layers for both samples, the hollow-shaped regions are prominently distributed under the brown corrosion products, leaving the near-intact steel substrate under the relatively flat rust layers. The hollow-shaped regions are supposed to act as the anodic sites during cyclic corrosion, and the proportion of such regions on the sample under $AlCl_3$ is greater than mixed salts. It is generally recognized that the corrosion processes proceed under electrolyte layers according to the iron dissolution in the anodic site and ORR in the cathodic site. With the anodic iron dissolution, a proportion of iron ions is supposed to hydrolyze and induce localized acidification in the anodic sites [5,38,39]:

$$4Fe^{2+} + O_2 + 6H_2O \rightarrow 4FeOOH + 8H^+ \quad (2)$$

$$Fe^{3+} + 3H_2O \rightarrow Fe(OH)_3 + 3H^+ \quad (3)$$

which is considered prominent sources for hydrogen evolution and absorption during cyclic corrosion. These findings indicate that $AlCl_3$ demonstrate a contributing role in localized corrosion and acidification during the cyclic corrosion process, which facilitates hydrogen entry into steel.

Combining the results of surface observation and hydrogen permeation, although an apparent dissolution of iron appears in the central area (Fig. 4(b), white arrow) under the droplet due to the difference in oxygen concentration, the hydrolysis of metal cations is not expected to produce a local acid environment as the pH buffering effect of the droplet. As water evaporates, the increase in the concentration of Cl^- will result in a local breakdown of the precipitated film and induce the anodic dissolution of iron underneath the brown corrosion products (Fig. 4(b), yellow arrows). In this case, the localized corrosion and hydrolysis reactions of metal cations are expected to facilitate the generation of absorbed hydrogen.

To corroborate the finding that $AlCl_3$ facilitate localized corrosion, the cross-sectional samples of the corroded surface under 3.33 mM $AlCl_3$ were prepared. The rust spot in the central area and the ring-shaped rust layer on the edge side of the corroded surface were selected as cutting positions for analysis. As shown in Fig. 7(a), a pronounced corrosion pit develops underneath the rust layers in the central area, showing a cavity structure with porous corrosion products. Apart from the serious central pit, the corroded surface in the central area is mainly composed of porous pits and thin rust layers. These porous structures are expected to provide significant venues for the deposited salts to deliquesce and initiate corrosion underneath the rust layers.

On the other hand, the edge side of the corroded surface is suggested as the cathodic site during the droplet corrosion process, where corrosion products prefer to accumulate. The thickness of the rust layers is significantly greater than that near the central area of the corroded surface, as shown in Fig. 7(b). In addition, the rust layers show a compact structure rather than a porous one formed in the central area. Notably, a corrosion pit filled with

corrosion products can be found under the rust layer, indicating that the edge side of the exposed surface is expected to develop new anodic sites during cyclic corrosion. It is notable that the pit depth under the thick rust layers on the edge side is less than that near the central area. As the presence of electrolytes introduced by the deposited salts is essential for corrosion to proceed and the thick rust is expected to obstruct the diffusion of moisture, the activity of the anodic dissolution of steel under the thick rust layers is suggested to be sluggish.

Together, the anodic dissolution begins due to the initial geometric shape of the droplets and proceeds under the rust layers. After the droplet evaporates, the localized dissolution of iron and hydrolysis reactions of metal cations produce an acidic environment under the rust layers, facilitating hydrogen entry into steel. As the wet-dry cycle proceeds, the processes of iron dissolution and the combined hydrolysis reactions of metal cations will be gradually retarded due to the increasing thickness of the rust layers.

3.6 Analysis of the corroded surfaces using SEM-EDS and AES

The SEM observation and EDS analysis were performed on the sample corroded under the $AlCl_3$ droplet and the results are presented in Fig. 8. The corroded surface is composed of hump-shaped products and relatively flat layers. The EDS mapping demonstrates the presence of Al and Cl elements on the corroded surface. Of note, Cl elements are particularly abundant in the hump-shaped corrosion products, while Al elements are enriched in some circular spots on the flat layers, as indicated by yellow arrows in Fig. 8(b). Fig. 8(c) presents the characteristic of the Al-rich structure, which is a raised spot surrounded by a ring of corrosion

products. These results imply that the Al and Cl elements are distributed separately during the corrosion processes. Al-rich area is supposed to be the cathodic site, while the Cl-rich area is the anodic site.

To further investigate the thin rust layers, AES analysis was carried out on the flat region of the corroded surface. Note that the sample was washed with ultrapure water before the analysis. Fig. 9(a) shows an area of the flat region, which is composed of a uniform rust layer and some raised corrosion products. As shown in the AES spectra (Fig. 9(b)), Al elements are detected in the uniform rust layer but not in the raised structures. In addition, a comparison of the auger spectra of Al with the Al_2O_3 peak of the standard spectra demonstrates that Al exists in the form of Al oxide (Fig. 9(c)). These results validate the precipitation of Al compounds during cyclic corrosion.

3.7 Proposed models for hydrogen entry into steel under $AlCl_3$ droplet during cyclic corrosion

The experimental results demonstrate the presence of hydrogen evolution and absorption during the cyclic corrosion of steel under salt droplets. Al^{3+} plays a significant role in the corrosion morphology and hydrogen entry into steel during the corrosion processes under the initial droplet and after the droplet evaporates.

The corrosion process and hydrogen entry into steel under the $AlCl_3$ droplet is illustrated in Fig. 10(a). Attributing to the droplet shape, oxygen is easy to reach the edge of the droplet and establishes a concentration cell in the droplet. An important feature of droplet corrosion is the migration of ions in the conductive electrolytes to maintain charge neutrality between the anodic and cathodic sites. Regarding the corrosion processes under the $AlCl_3$ droplet, Cl^- is

expected to move towards the anodic site and accelerate the iron dissolution, while Al^{3+} migrates to the cathodic site where ORR is predominant. Unlike the NaCl droplet, where Na^{+} is considered to maintain the local alkaline environment at the cathode, Al^{3+} tends to form precipitates and buffer the pH in the cathodic area. As a result, the changes in the local chemistry suppress ORR and enhance HER as the dominant cathodic reaction, which accelerates hydrogen absorption into steel.

On the other hand, the concentration of Cl^{-} is supposed to increase as water evaporates, which induces the breakdown of the Al-containing films and the development of new localized corrosion sites on the steel surface. Accompanying the anodic dissolution, the hydrolysis of the released iron ions leads to a decrease in the pH in the anodic areas. As a result, the decrease in the pH of the local environments provides an increased driving force for HER assuming a constant corrosion potential, which has a promotion effect on hydrogen absorption into steel.

After the droplet evaporates (Fig. 10(b)), a greater proportion of the dissolved $AlCl_3$ accumulates along the peripheral regions of the initial droplet and forms a ring-shaped deposit. This phenomenon is attributed to the capillary flow in the droplet during water evaporation [34,40]. The deposited $AlCl_3$ particles absorb moisture with varying RH and introduce local corrosion cells on the steel surface. New pits develop through anodic dissolution underneath the rust layers, accompanied by the cathodic reactions in the outer corrosion products. Attributing to the high hygroscopic property of $AlCl_3$, electrolyte layers are readily available in the porous structures of the pits for further dissolution of the steel substrate. The development of localized corrosion facilitates the decrease in the local pH,

promoting HER and hydrogen entry into steel. However, as the increased thickness of the rust layers is supposed to retard the access of electrolytes to the steel surface, the corrosion processes and hydrogen entry into steel progressively decline with the increasing number of corrosion cycles.

Overall, the proposed models suggest that Al^{3+} accelerates hydrogen entry into steel by the means of precipitation of Al compounds in the cathodic region under the droplets and localized acidification at the anodic site underneath the rust layers. Moreover, the high hygroscopic property of $AlCl_3$ deposited after the droplets evaporate introduces electrolytes to the steel surfaces with increasing RH and facilitates the establishment of corrosion and hydrogen absorption processes, which will be retarded by the progressively thicker rust layers.

4. Conclusions

The hydrogen permeation behaviour of steel under salt droplets with varying Al^{3+} concentrations was investigated to explore the influence of Al^{3+} on hydrogen entry into steel during atmospheric corrosion. Several conclusions could be drawn:

(1) The concentration of Al^{3+} in the droplet has a pronounced effect on corrosion morphology and hydrogen absorption into steel during cyclic corrosion. The amount of permeated hydrogen through steel increased with increasing Al^{3+} concentrations.

(2) The steels under $AlCl_3$ were subjected to localized corrosion. The localized acidification under the rust layers is suggested to accelerate the hydrogen evolution and absorption into steel.

(3) Al^{3+} precipitated on the cathodes and promoted HER during the corrosion processes under $AlCl_3$ droplets. The Al-containing precipitated films are suggested to retard iron dissolution before the droplets evaporate.

(4) The hygroscopic property of $AlCl_3$ is one of the contributing factors for hydrogen entry into steel during cyclic corrosion. It is attributed to the low DRH of $AlCl_3$ that facilitates the formation of electrolytes.

(5) The hydrogen evolution and absorption processes are most prominent during the drying period of cyclic corrosion under salt droplets, which are retarded by the increase of thickness of rust layers as corrosion proceeds.

Acknowledgements

This work was supported by JST SPRING [Grant Number JPMJSP2119]. The authors acknowledge the research groups, “Comprehensive Understanding of Hydrogen-Passive Surface on Steels for Prevention of Hydrogen Embrittlement” and “Corrosion-induced Hydrogen Absorption to Steels” of the Iron and Steel Institute of Japan. A part of this work was conducted at the Laboratory of XPS analysis, Joint-use facilities, Hokkaido University, supported by “Advanced Research Infrastructure for Materials and Nanotechnology in Japan (ARIM)” of the Ministry of Education, Culture, Sports, Science and Technology (MEXT). Proposal Number JPMXP1222HK-0032.

References

[1] Z. Ahmad, ATMOSPHERIC CORROSION, in: Z. Ahmad (Ed.), Principles of corrosion engineering and corrosion control, Elsevier, 2006, pp. 550-575. https://doi.org/10.1016/B978-075065924-6/50011-8

[2] M.S. Azevedo, C. Allély, K. Ogle, P. Volovitch, Corrosion mechanisms of Zn (Mg, Al) coated steel in accelerated tests and natural exposure: 1. The role of electrolyte composition in the nature of corrosion products and relative corrosion rate, Corros. Sci. 90 (2015) 472-481. https://doi.org/10.1016/j.corsci.2014.05.014

[3] D. Thierry, D. Persson, G. Luckeneder, K.H. Stellnberger, Atmospheric corrosion of ZnAlMg coated steel during long term atmospheric weathering at different worldwide exposure sites, Corros. Sci. 148 (2019) 338-354. https://doi.org/10.1016/j.corsci.2018.12.033

[4] G. Lazorenko, A. Kasprzhitskii, T. Nazdracheva, Anti-corrosion coatings for protection of steel railway structures exposed to atmospheric environments: a review, Constr. Build. Mater. 288 (2021) 123115. https://doi.org/10.1016/j.conbuildmat.2021.123115

[5] T. Tsuru, Y. Huang, M.R. Ali, A. Nishikata, Hydrogen entry into steel during atmospheric corrosion process. Corros. Sci. 47 (2005) 2431-2440. https://doi.org/10.1016/j.corsci.2004.10.006

[6] E. Akiyama, S. Li, T. Shinohara, Z. Zhang, K. Tsuzaki, Hydrogen entry into Fe and high strength steels under simulated atmospheric corrosion, Electrochim. Acta 56 (2011) 1799-1805. https://doi.org/10.1016/j.electacta.2010.09.043

[7] S. Ootsuka, S. Fujita, E. Tada, A. Nishikata, T. Tsuru, Evaluation of hydrogen absorption

into steel in automobile moving environments, Corros. Sci. 98 (2015) 430-437. https://doi.org/10.1016/j.corsci.2015.05.049

[8] S. Ajito, E. Tada, A. Ooi, A. Nishikata, Hydrogen Absorption Behavior of Pre-Rusted Steels under an NaCl Droplet, J. Electrochem. Soc. 166 (2019) C243. https://doi.org/10.1149/2.0591910jes

[9] X. Han, M. Sakairi, Hydrogen permeation behavior of steel under wet/dry corrosion with changes in relative humidity at the dry period, ISIJ Int. 61 (2021) 1194-1200. https://doi.org/10.2355/isijinternational.ISIJINT-2020-555

[10] T. Omura, Hydrogen entry and its effect on delayed fracture susceptibility of high strength steel bolts under atmospheric corrosion, ISIJ Int. 52 (2012) 267-273. https://doi.org/10.2355/isijinternational.52.267

[11] I.S. Cole, W.D. Ganther, J.D. Sinclair, D. Lau, D.A. Paterson, A study of the wetting of metal surfaces in order to understand the processes controlling atmospheric corrosion, J. Electrochem. Soc. 151 (2004) B627. https://doi.org/10.1149/1.1809596

[12] S. Hœrlé, F. Mazaudier, P. Dillmann, G. Santarini, Advances in understanding atmospheric corrosion of iron. II. Mechanistic modelling of wet–dry cycles, Corros. Sci. 46 (2004) 1431-1465. https://doi.org/10.1016/j.corsci.2003.09.028

[13] S.T. Martin, Phase transitions of aqueous atmospheric particles. Chem Rev. 100 (2000) 3403-3454. https://doi.org/10.1021/cr990034t

[14] E. Schindelholz, B.E. Risteen, R.G. Kelly, Effect of relative humidity on corrosion of steel under sea salt aerosol proxies: I. NaCl, J. Electrochem. Soc. 161 (2014) C450-C459. https://doi.org/10.1149/2.0221410jes

[15] E. Schindelholz, B.E. Risteen, R.G. Kelly, Effect of relative humidity on corrosion of steel under sea salt aerosol proxies: II. MgCl2, artificial seawater, J. Electrochem. Soc. 161 (2014) C460-C470. https://doi.org/10.1149/2.0231410jes

[16] G. Schimo-Aichhorn, I. Traxler, A. Muhr, C. Commenda, D. Rudomilova, O. Schneeweiss, G. Luckeneder, H. Duchaczek, K.H. Stellnberger, J. Faderl, T. Prošek, Hydrogen Insertion into Complex-Phase High-Strength Steel during Atmospheric Corrosion at Low Relative Humidity, Metals 12 (2022) 624. https://doi.org/10.3390/met12040624

[17] D.B. Blücher, J.E. Svensson, L.G. Johansson, The influence of CO2, AlCl3· 6H2O, MgCl2· 6H2O, Na2SO4 and NaCl on the atmospheric corrosion of aluminum. Corros. Sci. 48 (2006) 1848-1866. https://doi.org/10.1016/j.corsci.2005.05.027

[18] S. Mahmood, C. Gallagher, D.L. Engelberg, Atmospheric corrosion of aluminum alloy 6063 beneath ferric chloride corrosion product droplets, Corrosion, 76 (2020) 985-994. https://doi.org/10.5006/3558

[19] J. Alcántara, D. de la Fuente, B. Chico, J. Simancas, I. Díaz, M. Morcillo, Marine atmospheric corrosion of carbon steel: A review. Materials 10 (2017) 406. https://doi.org/10.3390/ma10040406

[20] R. Lindström, J.E. Svensson, L.G. Johansson, The influence of salt deposits on the atmospheric corrosion of zinc. The important role of the sodium ion, J. Electrochem. Soc. 149 (2002) B57. https://doi.org/10.1149/1.1432670

[21] T. Prosek, D. Thierry, C. Taxén, J. Maixner, Effect of cations on corrosion of zinc and carbon steel covered with chloride deposits under atmospheric conditions, Corros. Sci. 49

(2007) 2676-2693. https://doi.org/10.1016/j.corsci.2006.11.004

[22] C. Liu, V.A. Yang, R.G. Kelly, Inhibition of Cathodic Kinetics by Zn2+ and Mg2+ on AA7050-T7451, J. Electrochem. Soc. 166 (2019) C134. http://doi.org/10.1149/2.0551906jes

[23] R.M. Katonaab, R.G. Kelly, C.R. Bryana, R.F. Schallera, A.W. Knight, Use of in situ Raman spectroelectrochemical technique to explore atmospheric corrosion in marine-relevant environments, Electrochem. Commun. 118 (2020) 106768. https://doi.org/10.1016/j.elecom.2020.106768

[24] S. Zhang, T. Shibata, T. Haruna, Inhibition effect of metal cations to intergranular stress corrosion cracking of sensitized Type 304 stainless steel, Corros. Sci. 47 (2005) 1049-1061. https://doi.org/10.1016/j.corsci.2004.06.014

[25] T. Shibata, Passivity breakdown and stress corrosion cracking of stainless steel, Corros. Sci. 49 (2007) 20-30. https://doi.org/10.1016/j.corsci.2006.05.031

[26] M. Sakairi, R. Sasaki, A. Kaneko, Y. Seki, D. Nagasawa, Evaluation of metal cation effects on galvanic corrosion behavior of the A5052 aluminum alloy in low chloride ion containing solutions by electrochemical noise impedance, Electrochim. Acta, 131 (2014) 123-129. https://doi.org/10.1016/j.electacta.2014.02.010

[27] K. Otani, M. Sakairi, Effects of metal cations on corrosion of mild steel in model fresh water, Corros. Sci. 111(2016) 302-312. https://doi.org/10.1016/j.corsci.2016.05.020

[28] M.S. Islam, K. Otani, M. Sakairi, Effects of metal cations on mild steel corrosion in 10 mM Cl- aqueous solution, Corros. Sci. 131 (2018) 17-27. https://doi.org/10.1016/j.corsci.2017.11.015

[29] C. Liu, P. Khullar, R.G. Kelly, Acceleration of the cathodic kinetics on aluminum alloys by aluminum ions, J. Electrochem. Soc. 166 (2019) C153. http://doi.org/10.1149/2.0571906jes

[30] R.M. Katona, J.C. Carpenter, A.W. Knight, C.R. Bryan, R.F. Schaller, R.G. Kelly, E.J. Schindelholz, Importance of the hydrogen evolution reaction in magnesium chloride solutions on stainless steel, Corros. Sci. 177 (2020) 108935. https://doi.org/10.1016/j.corsci.2020.108935

[31] C.R. Bryan, A.W. Knight, R.M. Katona, A.C. Sanchez, E.J. Schindelholz, R.F. Schaller, Physical and chemical properties of sea salt deliquescent brines as a function of temperature and relative humidity. Sci. Total Environ. 824 (2022) 154462. https://doi.org/10.1016/j.scitotenv.2022.154462

[32] T. Tsuru, K.I. Tamiya, A. Nishikata, Formation and growth of micro-droplets during the initial stage of atmospheric corrosion, Electrochim. Acta, 49 (2004) 2709-2715. https://doi.org/10.1016/j.electacta.2004.01.032

[33] S. Li, L.H. Hihara, Atmospheric-corrosion electrochemistry of NaCl droplets on carbon steel, J. Electrochem. Soc.159 (2012) C461. http://doi.org/10.1149/2.035211jes

[34] V. Soulié, F. Lequien, F. Ferreira-Gomes, G. Moine, D. Feron, P. Prene, H. Moehwald, T. Zemb, H. Riegler, Salt-induced iron corrosion under evaporating sessile droplets of aqueous sodium chloride solutions. Mater. Corros. 68 (2017) 927-934. https://doi.org/10.1002/maco.201609319

[35] B.G. Koushik, N. Van den Steen, M.H. Mamme, Y. Van Ingelgem, H. Terryn, Review on modelling of corrosion under droplet electrolyte for predicting atmospheric corrosion

rate. J. Mater. Sci. Technol., 62 (2021) 254-267. https://doi.org/10.1016/j.jmst.2020.04.061

[36] U.R. Evans, Mechanism of rusting, Corros. Sci. 9 (1969) 813-821. https://doi.org/10.1016/S0010-938X(69)80074-0

[37] U.R. Evans, C.A.J. Taylor, Mechanism of atmospheric rusting, Corros. Sci. 12 (1972) 227-246. https://doi.org/10.1016/S0010-938X(72)90671-3

[38] J.R. Galvele, Transport processes and the mechanism of pitting of metals, J. Electrochem. Soc. 123 (1976) 464. https://doi.org/10.1149/1.2132857

[39] Y. Huang, Y. Zhu, Hydrogen ion reduction in the process of iron rusting, Corros. Sci. 47 (2005) 1545-1554. https://doi.org/10.1016/j.corsci.2004.07.044

[40] R.D. Deegan, O. Bakajin, T.F. Dupont, G. Huber, S.R. Nagel, T.A. Witten, 1997. Capillary flow as the cause of ring stains from dried liquid drops, Nature, 389 (1997) 827-829. https://doi.org/10.1038/39827

Figure Captions

Fig. 1 Schematic drawing of the experimental procedures.

Fig. 2 Typical change in hydrogen permeation current density of the sample exposed to the droplet of 3.33 mM $AlCl_3$ solution during (a) the first cycle and (b) the subsequent cycles of the cyclic corrosion test.

Fig. 3. Comparison of electric charges of the samples during (a) the first cycle and (b) the subsequent cycles as a function of the concentration of Al^{3+} in the salt solutions. Error bars represent one standard deviation.

Fig. 4. Optical images of corrosion morphology of the samples under (a) 1 mM $AlCl_3$ + 7 mM NaCl and (b) 3.33 mM $AlCl_3$ during cyclic corrosion.

Fig. 5. Polarization curves of the samples subjected to corrosion at different stages of the initial wet-dry cycle.

Fig. 6. Optical images of the corroded and rust-removed samples under (a) 1 mM $AlCl_3$ + 7 mM NaCl and (b) 3.33 mM $AlCl_3$ after 12 wet-dry cycles.

Fig. 7. Cross-sectional images of (a) the centre and (b) the edge of the rust layers formed on

the samples under $AlCl_3$ droplets after 12 wet-dry cycles.

Fig. 8. SEM-EDS images of the sample under $AlCl_3$ droplet after 12 wet-dry cycles. (a) SEM image of the corrosion products on the sample. (b) SEM image of an expanded area in (a) and the corresponding EDS mapping images of Fe, O, Al, and Cl. (c) SEM-EDS image of an Al-rich area in (a). Yellow arrows indicate the Al-rich areas.

Fig. 9. (a) A detailed SEM image of a flat area of the corroded surface in Fig. 8(a). (b) AES spectra of the selected points in (a). (c) Comparison of the detected AES spectra in the Al spectral range with the standard spectra.

Fig. 10. Schematic description of the corrosion process and hydrogen absorption into steel (a) under the $AlCl_3$ droplet and (b) after water evaporation. H_{ad} and H_{ab} indicate adsorbed hydrogen and absorbed hydrogen.

Table

Table 1. The composition and pH of the salt solutions in the experiment.

Solution	Composition	pH
1	3.3 mM $AlCl_3 \cdot 6H_2O$	4.03
2	2.5 mM $AlCl_3 \cdot 6H_2O$ + 2.5 mM NaCl	4.10
3	1 mM $AlCl_3 \cdot 6H_2O$ + 7 mM NaCl	4.27
4	10 mM NaCl	5.75

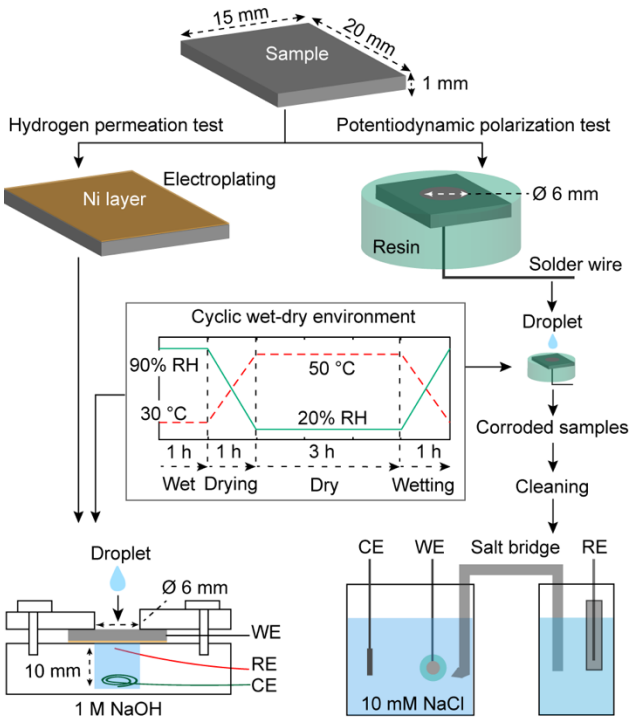

Fig. 1 Schematic drawing of the experimental procedures.

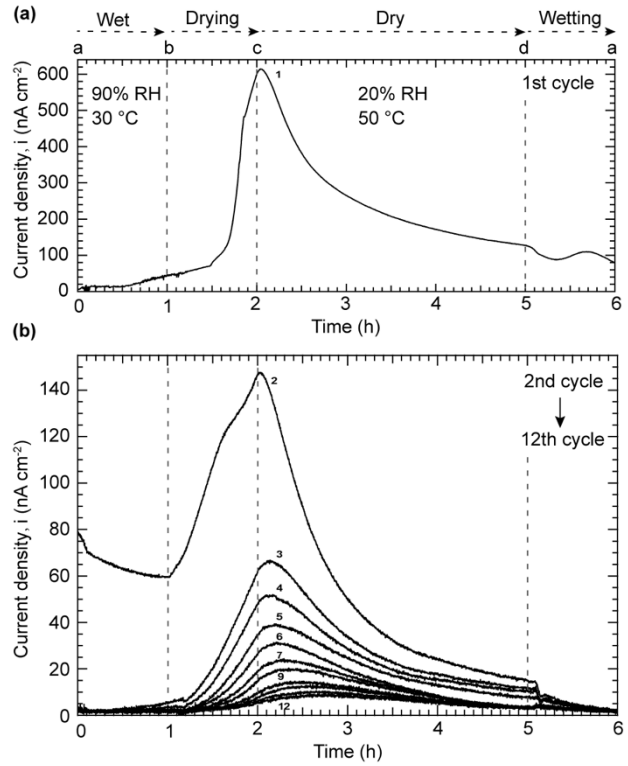

Fig. 2 Typical change in hydrogen permeation current density of the sample exposed to the droplet of 3.33 mM $AlCl_3$ solution during (a) the first cycle and (b) the subsequent cycles of the cyclic corrosion test.

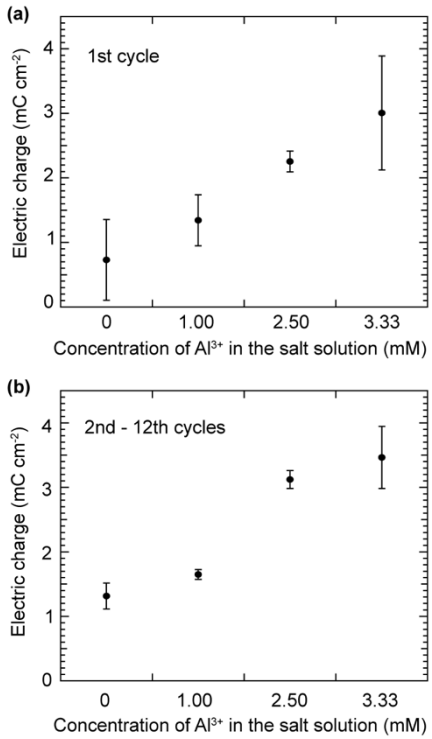

Fig. 3. Comparison of electric charges of the samples during (a) the first cycle and (b) the subsequent cycles as a function of the concentration of Al^{3+} in the salt solutions. Error bars represent one standard deviation.

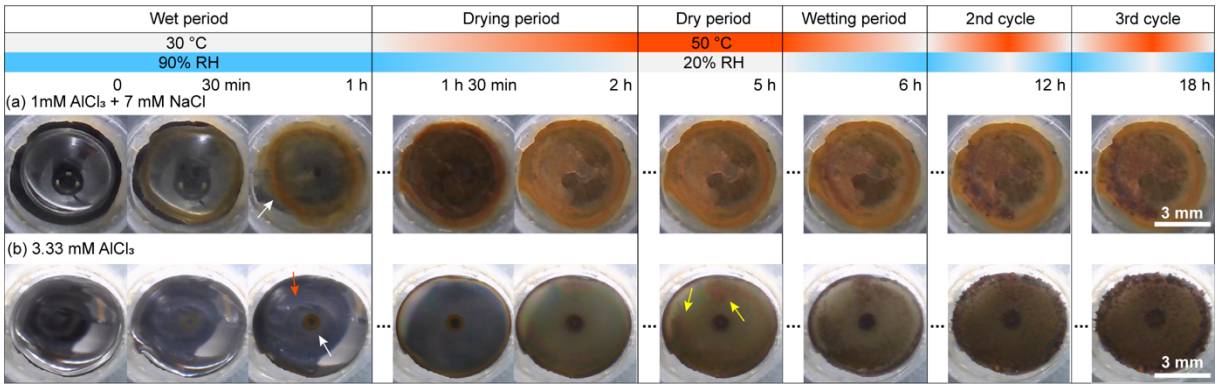

Fig. 4. Optical images of corrosion morphology of the samples under (a) 1 mM $AlCl_3$ + 7 mM NaCl and (b) 3.33 mM $AlCl_3$ during cyclic corrosion.

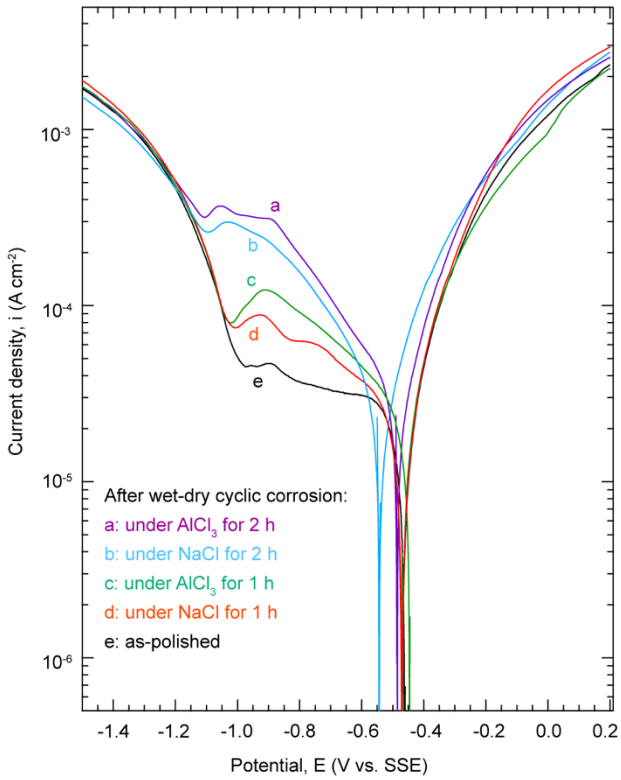

Fig. 5. Polarization curves of the samples subjected to corrosion at different stages of the initial wet-dry cycle.

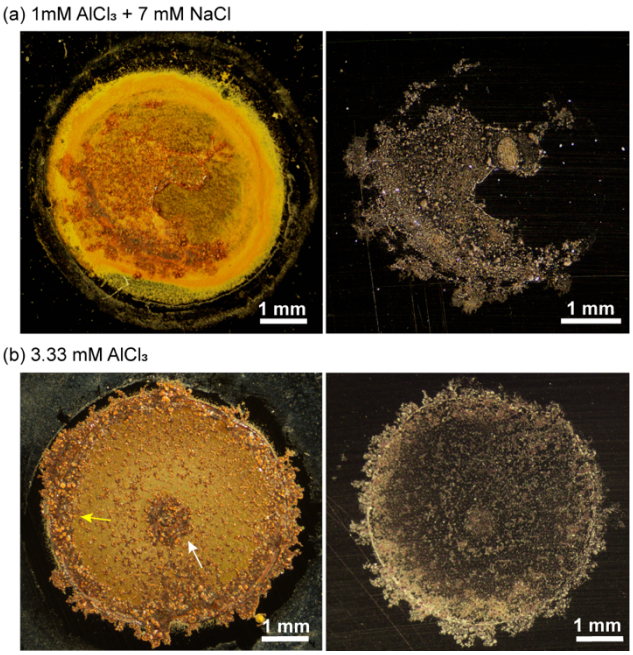

Fig. 6. Optical images of the corroded and rust-removed samples under (a) 1 mM $AlCl_3$ + 7 mM NaCl and (b) 3.33 mM $AlCl_3$ after 12 wet-dry cycles.

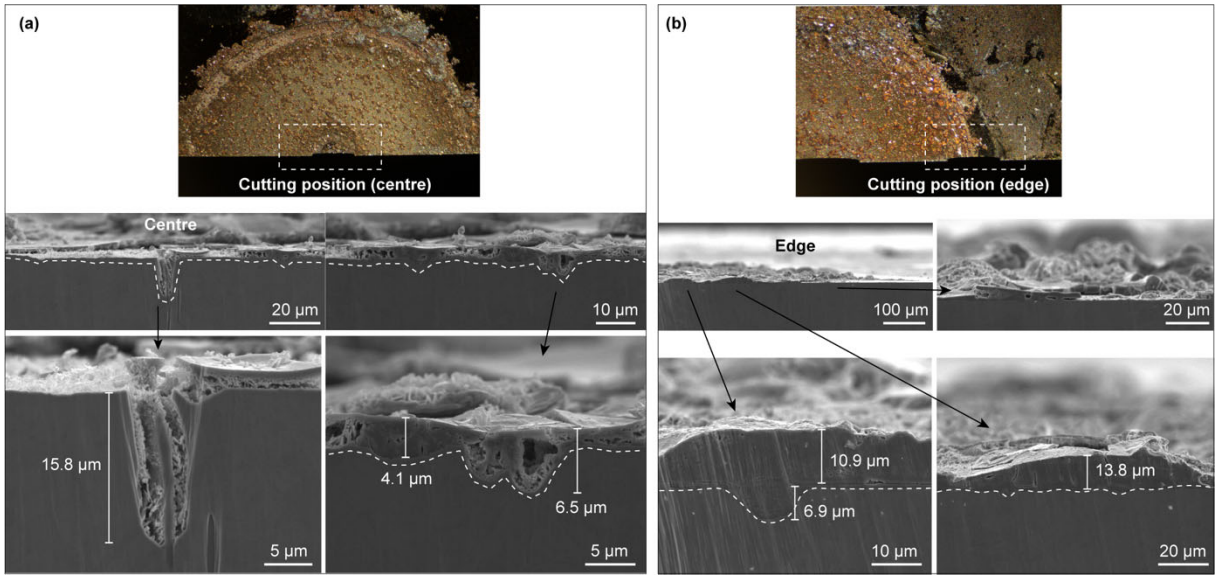

Fig. 7. Cross-sectional images of (a) the centre and (b) the edge of the rust layers formed on the samples under $AlCl_3$ droplets after 12 wet-dry cycles.

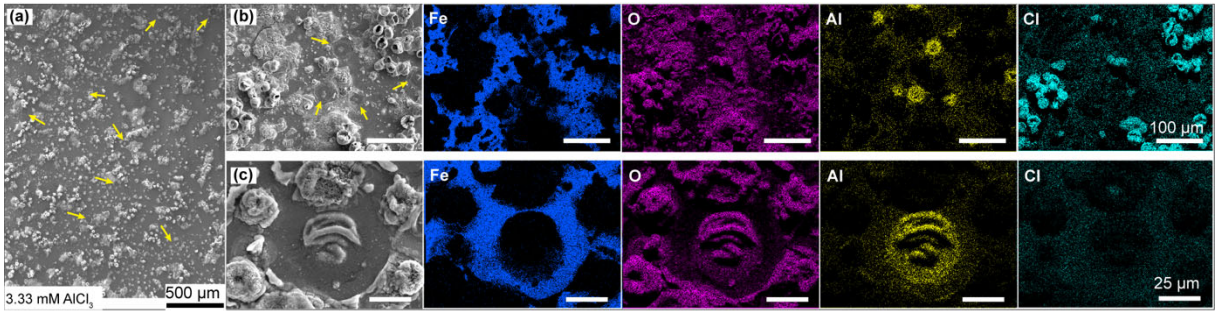

Fig. 8. SEM-EDS images of the sample under $AlCl_3$ droplet after 12 wet-dry cycles. (a) SEM image of the corrosion products on the sample. (b) SEM image of an expanded area in (a) and the corresponding EDS mapping images of Fe, O, Al, and Cl. (c) SEM-EDS images of an Al-rich area in (a). Yellow arrows indicate the Al-rich areas.

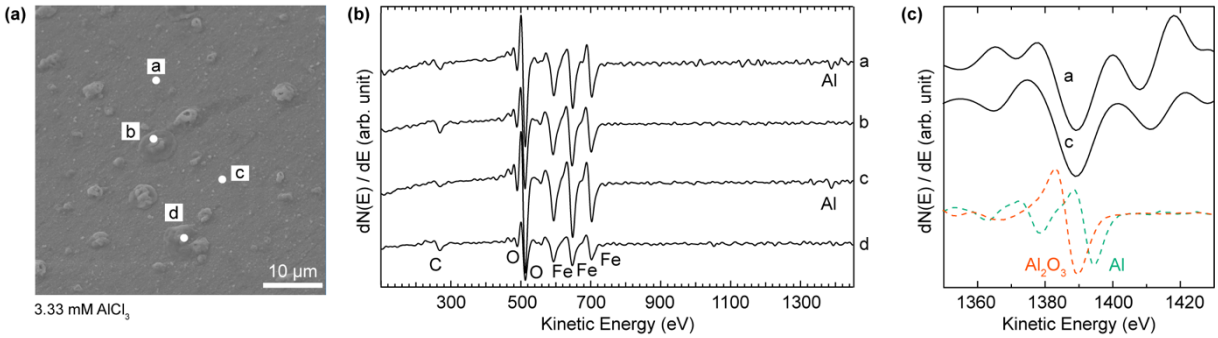

Fig. 9. (a) A detailed SEM image of a flat area of the corroded surface in Fig. 8(a). (b) AES spectra of the selected points in (a). (c) Comparison of the detected AES spectra in the Al spectral range with the standard spectra.

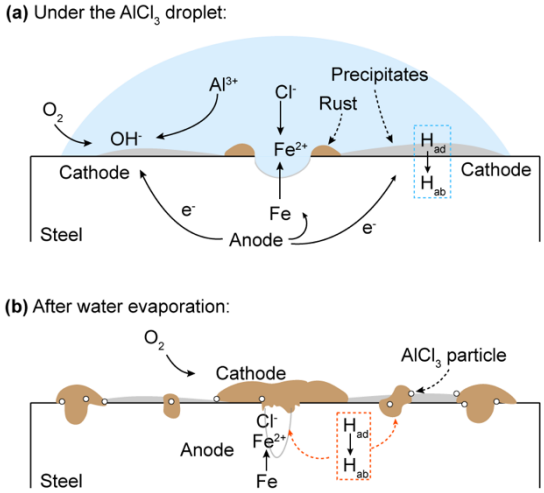

Fig. 10. Schematic description of the corrosion process and hydrogen absorption into steel (a) under the $AlCl_3$ droplet and (b) after water evaporation. H_{ad} and H_{ab} indicate adsorbed hydrogen and absorbed hydrogen.